arXiv:2203.08710v1 [cond-mat.mes-hall] 16 Mar 2022

Potential nanoscale sources of decoherence in niobium based transmon qubit architectures

Akshay A. Murthy[1*] , Paul Masih Das[2], Stephanie M. Ribet[2,3], Cameron Kopas[4], Jaeyel Lee[1], Matthew J. Reagor[4], Lin Zhou[5], Matthew J. Kramer[5], Mark C. Hersam[2,6,7], Mattia Checchin[1], Anna Grassellino[1], Roberto dos Reis[2,3,8], Vinayak P. Dravid[2,3,8*], Alexander Romanenko[1*]

[1] *Superconducting Quantum Materials and Systems Center, Fermi National Accelerator Laboratory (FNAL), Batavia, IL 60510, USA*

[2] *Department of Materials Science and Engineering, Northwestern University, Evanston, IL 60208, USA*

[3] *International Institute of Nanotechnology, Northwestern University, Evanston, IL 60208, USA*

[4] *Rigetti Computing, Berkeley, CA 94710, USA*

[5] *Ames Laboratory, U.S. Department of Energy, Ames, IA 50011, United States*

[6] *Department of Chemistry, Northwestern University, Evanston, IL 60208*

[7] *Department of Electrical and Computer Engineering, Northwestern University, Evanston, IL 60208 ,*

[8] *The NUANCE Center, Northwestern University, Evanston, IL 60208, USA*

(Dated: March 17, 2022)

Superconducting thin films of niobium have been extensively employed in transmon qubit architectures. Although these architectures have demonstrated remarkable improvements in recent years, further improvements in performance through materials engineering will aid in large-scale deployment. Here, we use information retrieved from electron microscopy and analysis to conduct a detailed assessment of potential decoherence sources in transmon qubit test devices. In the niobium thin film, we observe the presence of localized strain at interfaces, which may amplify interactions between two-level systems and impose limits on T_1 and T_2 relaxation times. Additionally, we observe the presence of a surface oxide with varying stoichiometry and bond distances, which can generate a broad two-level system noise spectrum. Finally, a similarly disordered and rough interface is observed between Nb and the Si substrate. We propose that this interface can also degrade the overall superconducting properties.

Keywords: superconducting qubits, 4D-STEM, electron diffraction, Nb thin films, interfaces, hydrides, decoherence mechanisms

I. INTRODUCTION

Over the last two decades, many significant advances have been made towards constructing large-scale quantum computers. In particular, superconducting quantum information technology has emerged as a leading architecture to interrogate complex problems commonly deemed intractable with the most efficient classical computing platforms [1–4]. Nonetheless, extending this technology to large-scale devices requires continued progress to improve reliability and performance. For instance, although improvements in quantum bit (qubit) designs and fabrication procedures over the past decade have led to remarkable two-qubit gate fidelities of 99.5%, a measure of how resistant a quantum operation is to decoherence[5], fidelities far beyond 99.9% are likely required for large-scale devices in noisy intermediate scale quantum (NISQ) applications such as exploring many-body problems [3]. Similarly, an order of magnitude improvement in T_1 energy relaxation and T_2 dephasing coherence times are also likely required to achieve this goal [6]. Such improvements require higher quality materials and specifically, an increased understanding and control over imperfections [7]. In previous studies, establishing form-function relationships in these materials, interfaces and surfaces have emerged as having the largest impact on performance.

As an example, in the case of niobium (Nb)-superconducting transmon qubits, the amorphous surface oxides that form upon ambient exposure serve as major sources of electromagnetic energy dissipation. At milliKelvin (mK) operating temperatures, they also display loss tangent values that are three orders of magnitude larger compared to the Nb thin films and Si substrates [8–10]. This loss can be largely attributed to two-state defects in the amorphous surface oxide, i.e. two-level system (TLS) defects [8]. These states emerge as a result of deviations from long-range order. The system is able to transition between the two states through low energy excitations [11, 12]. Because TLS are particularly problematic at low temperatures, where low energy excitations remain unsaturated, they serve as a primary noise mechanism and introduce decoherence at

* Correspondence email address: amurthy@fnal.gov, v-dravid@northwestern.edu, aroman@fnal.gov

This manuscript has been authored by Fermi Research Alliance, LLC under Contract No. DE-AC02-07CH11359 with the U.S. Department of Energy, Office of Science, Office of High Energy Physics.

the operating temperatures for superconducting transmon qubits.

The presence of grain boundaries within the Nb film decreases mean free paths and superconducting parameters, such as the residual-resistance ratio (RRR), which may be linked to T_1 energy relaxation decoherence times, these linear defects also require close monitoring [11]. As a result, it is important to understand the form-function relationships between processing parameters and structure and concentration of TLS defects in these materials. With this systematic study, we aim at providing an opportunity to to pinpoint and link particular structural and chemical features to potential mechanisms giving rise to TLS, such as tunneling atoms[13], tunneling electrons[14], and paramagnetic spins[15].

Over the years, a combination of various spectroscopy and microscopy techniques have led researchers to understand that deviations from crystalline range order on the nanoscale dictate quantum decoherence [12]. As such, electron microscopy is an indispensable tool for identification of materials that host TLS defects in a broader effort to eliminate these sources. Namely, the ability to procure a variety of analytical and spectroscopic signals from nanometric volumes with scanning transmission electron microscopy (STEM) allows for detection of chemical, structural, and electromagnetic fluctuations on these relevant length scales [16, 17]. In this study, we deploy STEM imaging and diffraction methods to pinpoint specific nanoscale defects in the Nb film and associated surfaces and interfaces within a transmon qubit test device. The use of cutting edge techniques to disentangle amorphous and crystalline features allows us to establish form-function relationships across technologically relevant heterogeneous interfaces. We observe a number of structural and chemical features in this system that can potentially serve as hosts for TLS and reduce performance. These include the presence of localized strain at interfaces, variation in bond distances in the disordered surface oxide layer, as well as a rough and diffuse metal/substrate interface.

II. EXPERIMENTAL

Nb films were prepared on Si (001) wafers (float-zone >10,000 Ohm-cm) via high-power impulse magnetron sputtering (HiPIMS) with a base pressure less than 1E-8 Torr at room temperature. Prior to deposition, the wafer was prepared with an RCA surface treatment detailed previously [18, 19]. Following Nb deposition, transmon qubits were fabricated following the procedures detailed by Nersisyan *et al.* [19].

TEM samples were prepared from the Nb capacitance pad indicated with the black box in Figure 1a using a 30 kV focused Ga^+ ion beam. In order to protect the surface oxide during the ion milling process, the sample was first coated with 50 nm of Ni. The samples were finely polished to a thickness of roughly 50 nm using 5 kV and 2 kV Ga^+ ions in an effort to remove surface damage and amorphization in the regions of interest. S/TEM data was collected on JEOL 300F Grand ARM S/TEM using an accelerating voltage of 300kV for the Nb film. The camera length is set to 80 cm and the condenser aperture is selected to provide a convergence semi-angle of 10 mrad. Four-dimensional STEM (4DSTEM) data sets [16] were acquired in a 360 x 62 mesh (with pixel size of 3.33 nm) across the Nb films using a Gatan® OneView camera and synchronized using STEMx. In the case of the associated interfaces, an accelerating voltage of 80kV was selected to reduce beam damage in the amorphous compounds and data acquired using a Gatan® Stela hybrid-pixelated camera and condenser aperture was selected to provide a convergence semi-angle of 1.5 mrad for fluctuation electron microscopy measurements. This yields a probe size that is roughly 1 nm and allows for characterizing amorphous regions that are on the order of 5 nm in dimension. The resultant image was subsequently passed through a Gaussian filter with a filter size of 2 pixels to eliminate scanning distortions. STEM-EDS measurements were collected at 200kV using a JEOL Silicon Drift Detector (SDD) with a solid angle of 1.7 sr.

III. RESULTS

In an effort to identify particular structural or chemical features associated with theoretical TLS mechanisms, we first begin with an assessment of the nanostructure and strain distribution in the Nb thin film. Each of these aspects is suspected to impact the resultant TLS noise spectrum. As the surfaces and interfaces associated with Nb have also proven to dissipate electromagnetic energy, we then search for microscopic features and inhomogeneities in these regions that can potentially give rise to TLS.

A. Impact of interfaces and inhomogeneities in Nb film

An annular dark field (ADF) image of the cross-section taken from the contact pad of the transmon qubit using collection angles varying between 10 mrad to 70 mrad is provided in Figure 1b. In Figure 1c, an elemental map taken from this region using energy dispersive x-ray spectroscopy (EDS) confirms the presence of a Nb film on a Si substrate. In Figure 2a and b, bright field (BF) images taken when tilted along the Nb {111} zone axis are provided. From this image, we observe that columnar grains form which are characteristic of the HiPIMS process and are roughly 50 nm by 170 nm.

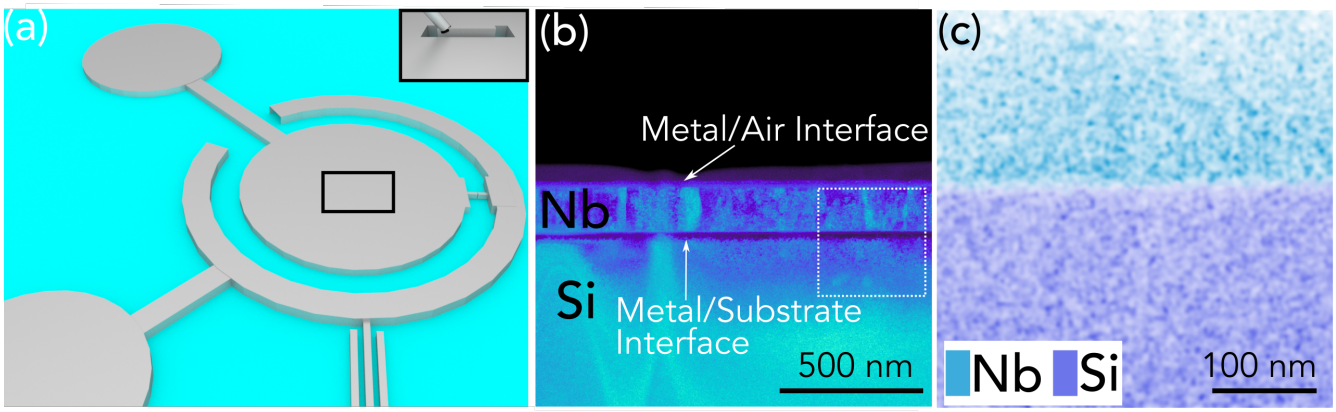

Figure 1. Nb/Si interface (a) Schematic of transmon qubit architecture. Black box represents the Nb contact pad region investigated in this study. (b) Annular dark field image taken from the cross-sectional TEM sample. The metal/air and metal/substrate interfaces discussed in Sections III B and III C are indicated. (c) EDS maps taken from the region indicated by the white box in (b) using characteristic Nb Lα and Si Kα x-ray emission.

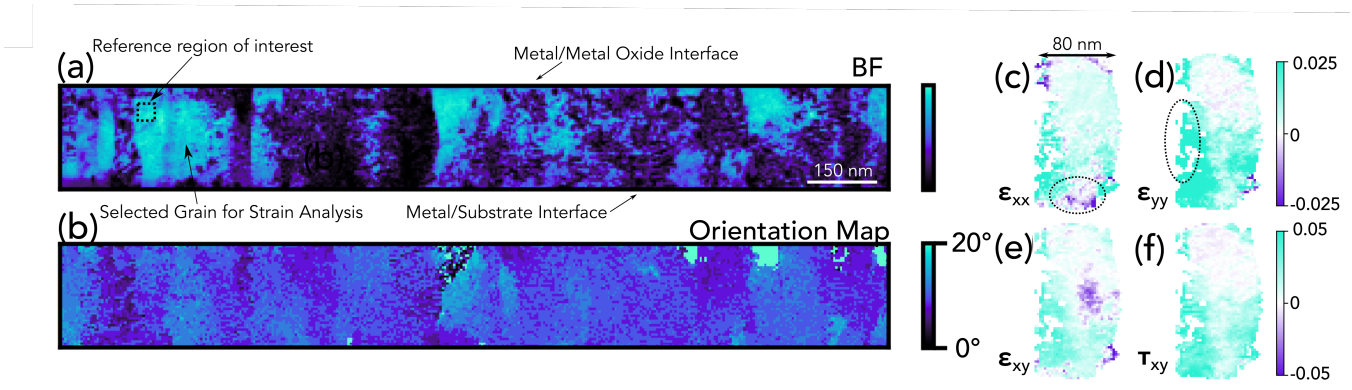

Figure 2. Nb film structure (a) Bright field and (b) Relative in-plane orientation map of Nb grains. Relative strain maps of an on-axis Nb grain are provided (c) along the substrate axis (ϵ_{xx}) and (d) along the film growth axis (ϵ_{yy}). Regions of compressive strain at the metal/substrate interface and tensile strain near the grain boundary are circled. Shear strain in the sample plane (ϵ_{xy}) along with rotational strain in the sample plane (τ_{xy}) are provided in (e) and (f) respectively. The selected grain and unstrained reference regions are also indicated.

It is also apparent that many of the grains are not oriented along this zone axis. In fact, from the orientation map, the grains tend to exhibit misorientation angles between 0 and 20 degrees from the Nb {111} zone axis in the sample plane. These columnar grains are separated by grain boundaries that exist parallel to the film growth axis.

Although a variety of chemical and physical properties contribute to BF contrast, strain is the dominant mechanism in this case due to large differences in the lattice constant between the metal and underlying substrate. In order to visualize these strained areas more clearly, we performed strain analysis using the algorithm detailed by Pekin *et al.* [20]. Strain within a crystalline sample leads to small atomic shifts in real space, which manifest in shifts to the diffraction pattern in reciprocal space. These shifts to the diffraction pattern can be measured and linked to relative in-plane strain in the sample through a transformation matrix. This approach is advantageous over direct real space mapping because it does not require the resolution and signal to noise necessary for atomic resolution imaging. The resultant strain maps in various directions are provided in Figures 2c-f for a representative grain oriented perfectly along the zone axis.

Along the substrate axis (ϵ_{xx}), we observe the presence of compressive strain at the metal/substrate interface which displays more tensile character in the direction towards the surface. The interfacial compressive strain can be attributed to surface stresses present

in this region [21]. Conversely, the tensile stress away from the interface likely arises from the coalescence of neighboring grains [22]. Meanwhile, the principal strain along the film growth axis (ϵ_{yy}), the shear strain in the sample plane (ϵ_{xy}) and the rotational strain in the sample plane (τ_{xy}) each exhibit similar profiles. Namely, the largest strains are concentrated near grain boundaries. This is likely due to the pileup of dislocations in this region to mediate a commensurate atomic structure between neighboring, but differently oriented grains [23]. This rotational commensurability of adjacent grains may also explain the presence of ϵ_{xy} strain in the film. In all cases, we find that the free surface mediates strain relaxation as the strain levels decay to zero in the direction towards the surface.

Nanometer sized grains with a variety of orientations may have implications for qubit performance. One possible mechanism for loss arises because grain boundary diffusion is likely the dominant route for solute migration in such systems. With a higher density of grain boundaries, impurity atoms have more paths to diffuse from the surface oxide into the Nb film. Other studies have demonstrated that oxygen atoms may preferentially segregate along grain boundaries in these systems, which may be correlated to reduced T_1 times [11]. Furthermore, because strain fields are found to localize at grain boundaries, their associated elastic dipoles can lead to interactions between neighboring TLS at the grain boundary [12]. These TLS interactions are known to generate TLS with variable frequencies, which makes device control far more challenging [24]. Moreover, lattice strain may induce localized changes in the critical temperature and superconducting order parameter[25], and highly strained regions may potentially trap non-equilibrium quasiparticles. These trapped quasiparticles have previously been demonstrated to behave similarly to other TLS mechanisms in systems exhibiting a spatially fluctuating superconducting order parameter, offering another potential source of decoherence in this system [26]. Thus, these potential loss mechanisms highlight the importance of manipulating the processing conditions as well as the underlying substrate to achieve Nb films with larger grains and improved device performance.

B. Role of Nb surface oxide

In addition to the Nb film, adjacent surfaces and interfaces are also known to impact the coherence properties in the system. As discussed in Section I, Nb surface oxides, which form spontaneously in ambient conditions, exhibit loss tangent values that are roughly three orders of magnitude larger than the surrounding film and crystalline substrate [8]. A dark field STEM image of this surface oxide and the associated thin film is provided in Figure 3a. This image was constructed by applying a virtual detector with an inner collection angle of 10 mrad and an outer collection angle of 15 mrad, which was designed specifically to match the initial diffraction ring observed in the NbO_x diffraction pattern (Figure S2). Representative diffraction patterns captured from the indicated regions in the dark field image in Figure 3a are provided in Figure 3d-h. The broad diffuse rings we observe are indicative of a lack of long-range order, which is problematic because it makes this oxide prone to hosting TLS defects.

Since the oxide region exhibits amorphous-like character in the diffraction pattern, we employ fluctuation electron microscopy (FEM) to better understand the medium range ordering present in the sample. This analysis was conducted following the approaches detailed by Kennedy *et al.* and Mu *et al.* [27, 28]. First, this process involves using a 1 nm probe and capturing diffraction patterns as a function of position. Following elliptical correction, radial fitting of amorphous rings in each diffraction pattern is subsequently performed using least squares regression. The radial intensity and normalized variance of the annular means were then calculated as a function of scattering angle. Additional details of this technique are provided in Appendix B.

Profiles of the normalized variance of the annular means for each indicated position in the dark field image are seen in Figure 3c. From these profiles, it is apparent that the position of the broad peak centered about roughly 5 nm^{-1} shifts to higher frequencies when moving in the direction away from the surface. Based on the limited symmetry observed in the diffraction patterns taken from the Nb oxide, the inverse of the peak positions in this profile were used to estimate the minimum bond distances in the surface oxide.[29] Based on this analysis, we find that this corresponds roughly to a bond distance of 2Å. This corresponds to an initial peak in the calculated radial distribution function profile for Nb_2O_5 (Figure S1) [30]. The radial distribution function represents the probability of locating an atom at a given radial distance, r, from the reference atom.

Further, we observe a steady decrease in this bond distance beginning at the top surface in the direction away from the surface as plotted in Figure 3b. The decrease in bond distance is suggestive of an increase in atomic density in the direction away from the surface. Based on the reported densities for NbO, NbO_2, and Nb_2O_5, this increase in atomic density may possibly be explained by an decrease in oxidation state of the Nb in the Nb oxide when moving in the direction away from the surface. This is in agreement with previous findings suggesting that whereas Nb_2O_5 has been observed at the surface, NbO_2 and NbO are observed closer to the Nb film [10, 11, 31]. We predict that this variation in bonding distances throughout the Nb oxide can lead to tunneling atoms/electrons imposing noise over a wide

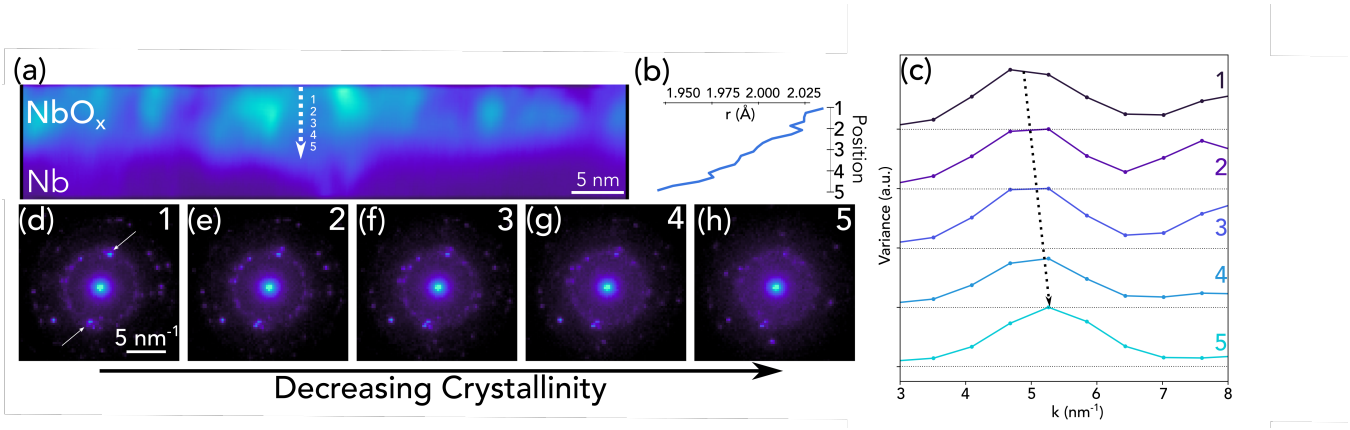

Figure 3. Nb/O interface (a) DF image of Nb oxide/Nb constructed using a virtual detector that matched the diffraction ring of Nb oxide seen in SI Figure 2b. (b) Variation in bond distance as a function of regions labeled 1-5 in the DF image. (c) Annular mean of normalized variances as a function of position. The peak positions are observed to red-shift from region 1 to region 5. The reciprocal of the peak positions in these plots were used to calculate the respective bond distances at each region. (d-h) Diffraction patterns taken from regions 1, 2, 3, 4, and 5, respectively. As the distinct diffraction spots indicated by the arrows fade in intensity from region 1 to region 5, it is apparent that the Nb oxide decreases in crystallinity in the direction away from the surface.

spectrum as opposed to a single frequency [13, 32].

In addition to the broad diffuse rings in the electron diffraction patterns in Figure 3d-h, we also observe a number of distinct diffraction spots. These are especially prevalent in the representative diffraction patterns taken from regions 1-3 before appearing to decay in intensity in the representative diffraction patterns taken from regions 4 and 5. This evolution in the diffraction pattern is observed throughout the film as highlighted in Figure S2. As the appearance of these distinct diffraction spots is indicative of ordering in the system, this suggests that the Nb oxide closest to the surface (Nb_2O_5) is more semi-crystalline in nature.

This is reasonable as oxygen diffusion is responsible for growth of the surface oxide. In this process, the oxygen concentration is expected to decay as a function of position in the direction from the top surface of the NbO_x to the Nb film. As such, regions closest to the surface have a higher likelihood of approaching an ordered and stoichiometric Nb_2O_5 state. Meanwhile, this mechanism for oxygen transport may cause regions closest to the Nb film to be amorphous and sub-stoichiometric as suggested by these findings. Due to the amorphous nature of the sub-oxide, as well as the fact that sub-oxides of niobium give rise to magnetic dipoles,[33] it is likely that in addition to the large loss tangent value of Nb_2O_5, regions 4 and 5 in Figure 3a play a critical role in introducing decoherence in the transmon qubit [34, 35].

C. Role of Nb/Si interface

The metal/substrate interface between Nb and Si may serve as a source of decoherence as well. In Figure 4a, a phase map of this interface is provided. This map was constructed using virtual annular detectors with collection angles of 40-45 mrad as well as 20-25 mrad for Nb and Si, respectively (Figure S3). The former were used to capture signal diffracted from the Nb{110} family of planes and the latter were used to capture signal diffracted from the Si{200} family of planes. The two resultant maps were overlaid upon one another to obtain a qualitative understanding of chemical distribution. Based on the slowly varying intensity gradients in the phase map, we observe that an Nb and Si form an alloy phase that exists between the metal and the substrate. Additionally, we also observe that the underlying Si substrate is very rough and has likely been altered by the buffered oxide etchant, which is used to remove Si oxide prior to Nb deposition.

Based on electron diffraction patterns taken across this interface, we define 3 distinct regions that exist between the crystalline Nb metal and Si substrate. Representative diffraction patterns taken from each of these indicated regions are provided in Figure 4b-d and representative diffraction patterns taken from the Nb film and the Si substrate are provided in Figure S3. Each of these regions display diffuse rings which are again indicative of a lack of long-range order. Based on the presence of intense diffraction spots associated with Nb along with weak diffraction spots associated with Si, we hypothesize that region 1 is an amorphous niobium sili-

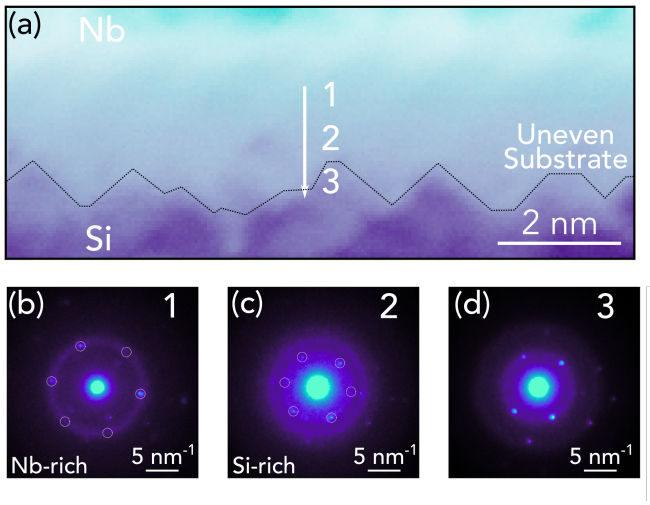

Figure 4. Nb/Si interface (a) Phase map of Nb and Si using virtual annular detectors shown in Figure S3. (b-d) Diffraction patterns taken from regions 1, 2, and 3, respectively.

cide region that is niobium rich in nature. Conversely through this analysis, region 2 is an amorphous niobium silicide region that appears to be silicon rich. Finally, although the diffraction pattern taken from also exhibits a diffuse ring, the consistency between the diffraction pattern taken from region 3 and the reference pattern taken from the Si substrate suggests that this region likely represents a semi-crystalline region of Si that has been roughened during various steps in the deposition and lithography process.

We hypothesize that structural properties in each of these regions should be investigated and improved for potential coherence benefits. For instance, regions 1 and 2 are amorphous regions, which may house TLS defects. Additionally, we would expect these niobium silicide regions to be non-superconducting, which would impact T_1 coherence times. Because region 3 exhibits significant surface roughness and disorder, we expect charge carriers in these regions to exhibit very low mean free paths, which may impact the superconductivity properties.

IV. SUMMARY & CONCLUSIONS

In this study, we applied STEM imaging and diffraction methods to identify structural inhomogeneities and defects within a test transmon device that may be linked to decoherence in Nb films and associated interfaces. In the Nb film, we observed grain sizes with the minimum dimension on the order of tens of nanometers, and localized strain at grain boundary interfaces. In the disordered niobium surface oxide layer, we observed a significant variation in the bond distances, and in the diffuse metal/substrate interface, we detected significant atomic disorder and surface roughness. These local structural and atomic features can lead to broad TLS frequency spectra, charge noise, and impact the superconducting parameters of the film. improving synthesis and processing parameters may lead to improved qubit performance. As such processes focused on achieving larger grains, eliminating the entire surface oxide, and obtaining an epitaxial metal/substrate interface are critical to obtaining improved qubit performance.

ACKNOWLEDGEMENTS

This material is based upon work supported by the U.S. Department of Energy, Office of Science, National Quantum Information Science Research Centers, Superconducting Quantum Materials and Systems Center (SQMS) under the contract No. DE-AC02-07CH11359. This work made use of the EPIC facility of Northwestern University's NU*ANCE* Center, which received support from the Soft and Hybrid Nanotechnology Experimental (SHyNE) Resource (NSF ECCS-1542205); the MRSEC program (NSF DMR-1720139) at the Materials Research Center; the International Institute for Nanotechnology (IIN); the Keck Foundation; and the State of Illinois, through the IIN. The authors thank members of the Superconducting Quantum Materials and Systems (SQMS) Center for valuable discussion. S. M. R. gratefully acknowledges support from IIN and 3M. The authors thank Dr. Anahita Pakzad from Ametek/Gatan, Inc, Pleasanton, CA, for the valuable feedback on the usage of the Stela pixelated detector.

[1] M. Kjaergaard, M. E. Schwartz, J. Braumüller, P. Krantz, J. I.-J. Wang, S. Gustavsson, and W. D. Oliver, Annual Review of Condensed Matter Physics **11**, 369 (2020), https://doi.org/10.1146/annurev-conmatphys-031119-050605.

[2] G. Wendin, Reports on Progress in Physics **80**, 106001 (2017).

[3] N. P. de Leon, K. M. Itoh, D. Kim, K. K. Mehta, T. E. Northup, H. Paik, B. S. Palmer, N. Samarth, S. Sangtawesin, and D. W. Steuerman, Science **372** (2021), 10.1126/science.abb2823.

[4] C. E. Murray, "Material matters in superconducting qubits," (2021), arXiv:2106.05919 [quant-ph].

[5] P. Jurcevic, A. Javadi-Abhari, L. S. Bishop, I. Lauer, D. F. Bogorin, M. Brink, L. Capelluto, O. Günlük, T. Itoko, N. Kanazawa, A. Kandala, G. A. Keefe, K. Krsulich, W. Landers, E. P. Lewandowski, D. T. McClure, G. Nannicini, A. Narasgond, H. M. Nayfeh, E. Pritchett, M. B. Rothwell, S. Srinivasan, N. Sundaresan, C. Wang, K. X. Wei, C. J. Wood, J.-B. Yau, E. J. Zhang, O. E. Dial, J. M. Chow, and J. M. Gambetta, Quantum Science and Technology **6**, 025020 (2021).

[6] C. Wang, X. Li, H. Xu, Z. Li, J. Wang, Z. Yang, Z. Mi, X. Liang, T. Su, C. Yang, G. Wang, W. Wang, Y. Li, M. Chen, C. Li, K. Linghu, J. Han, Y. Zhang, Y. Feng, Y. Song, T. Ma, J. Zhang, R. Wang, P. Zhao, W. Liu, G. Xue, Y. Jin, and H. Yu, "Transmon qubit with relaxation time exceeding 0.5 milliseconds," (2021), arXiv:2105.09890 [quant-ph].

[7] A. A. Murthy, J. Lee, C. Kopas, M. J. Reagor, A. P. McFadden, D. P. Pappas, M. Checchin, A. Grassellino, and A. Romanenko, Applied Physics Letters **120**, 044002 (2022), https://doi.org/10.1063/5.0079321.

[8] A. Romanenko, R. Pilipenko, S. Zorzetti, D. Frolov, M. Awida, S. Belomestnykh, S. Posen, and A. Grassellino, Phys. Rev. Applied **13**, 034032 (2020).

[9] C. R. H. McRae, H. Wang, J. Gao, M. R. Vissers, T. Brecht, A. Dunsworth, D. P. Pappas, and J. Mutus, Review of Scientific Instruments **91**, 091101 (2020), https://doi.org/10.1063/5.0017378.

[10] J. Verjauw, A. Potočnik, M. Mongillo, R. Acharya, F. Mohiyaddin, G. Simion, A. Pacco, T. Ivanov, D. Wan, A. Vanleenhove, L. Souriau, J. Jussot, A. Thiam, J. Swerts, X. Piao, S. Couet, M. Heyns, B. Govoreanu, and I. Radu, Phys. Rev. Applied **16**, 014018 (2021).

[11] A. Premkumar, C. Weiland, S. Hwang, B. Jaeck, A. P. M. Place, I. Waluyo, A. Hunt, V. Bisogni, J. Pelliciari, A. Barbour, M. S. Miller, P. Russo, F. Camino, K. Kisslinger, X. Tong, M. S. Hybertsen, A. A. Houck, and I. Jarrige, arXiv (2020), 2004.02908 [physics.app-ph].

[12] C. Müller, J. H. Cole, and J. Lisenfeld, Reports on Progress in Physics **82**, 124501 (2019).

[13] A. P. Paz, I. V. Lebedeva, I. V. Tokatly, and A. Rubio, Phys. Rev. B **90**, 224202 (2014).

[14] K. Agarwal, I. Martin, M. D. Lukin, and E. Demler, Phys. Rev. B **87**, 144201 (2013).

[15] E. Paladino, Y. M. Galperin, G. Falci, and B. L. Altshuler, Rev. Mod. Phys. **86**, 361 (2014).

[16] C. Ophus, Microscopy and Microanalysis **25**, 563–582 (2019).

[17] S. M. Ribet, A. A. Murthy, E. W. Roth, R. dos Reis, and V. P. Dravid, Materials Today (2021), https://doi.org/10.1016/j.mattod.2021.05.006.

[18] M. R. Vissers, J. Gao, D. S. Wisbey, D. A. Hite, C. C. Tsuei, A. D. Corcoles, M. Steffen, and D. P. Pappas, Applied Physics Letters **97**, 232509 (2010), https://doi.org/10.1063/1.3517252.

[19] A. Nersisyan, S. Poletto, N. Alidoust, R. Manenti, R. Renzas, C.-V. Bui, K. Vu, T. Whyland, Y. Mohan, E. A. Sete, S. Stanwyck, A. Bestwick, and M. Reagor, in *2019 IEEE International Electron Devices Meeting (IEDM)* (2019) pp. 31.1.1–31.1.4.

[20] T. C. Pekin, C. Gammer, J. Ciston, A. M. Minor, and C. Ophus, Ultramicroscopy **176**, 170 (2017), 70th Birthday of Robert Sinclair and 65th Birthday of Nestor J. Zaluzec PICO 2017 – Fourth Conference on Frontiers of Aberration Corrected Electron Microscopy.

[21] R. C. Cammarata, Progress in Surface Science **46**, 1 (1994).

[22] C. Wu, Thin Solid Films **64**, 103 (1979), international Conference on Metallurgical Coatings, San Diego, 1979-Part III.

[23] L. R. Nivedita, A. Haubert, A. K. Battu, and C. V. Ramana, Nanomaterials **10** (2020), 10.3390/nano10071287.

[24] L. Faoro and L. B. Ioffe, Phys. Rev. Lett. **109**, 157005 (2012).

[25] M. David Henry, S. Wolfley, T. Monson, B. G. Clark, E. Shaner, and R. Jarecki, Journal of Applied Physics **115**, 083903 (2014), https://doi.org/10.1063/1.4866554.

[26] S. E. de Graaf, L. Faoro, L. B. Ioffe, S. Mahashabde, J. J. Burnett, T. Lindström, S. E. Kubatkin, A. V. Danilov, and A. Y. Tzalenchuk, Science Advances **6**, eabc5055 (2020), https://www.science.org/doi/pdf/10.1126/sciadv.abc5055.

[27] E. Kennedy, N. Reynolds, L. Rangel DaCosta, F. Hellman, C. Ophus, and M. C. Scott, Applied Physics Letters **117**, 091903 (2020), https://doi.org/10.1063/5.0015532.

[28] X. Mu, D. Wang, T. Feng, and C. Kübel, Ultramicroscopy **168**, 1 (2016).

[29] T. F. Harrelson, E. Sheridan, E. Kennedy, J. Vinson, A. T. N'Diaye, M. V. P. Altoé, A. Schwartzberg, I. Siddiqi, D. F. Ogletree, M. C. Scott, and S. M. Griffin, Applied Physics Letters **119**, 244004 (2021), https://doi.org/10.1063/5.0069549.

[30] C. L. Farrow, P. Juhas, J. W. Liu, D. Bryndin, E. S. Božin, J. Bloch, T. Proffen, and S. J. L. Billinge, Journal of Physics: Condensed Matter **19**, 335219 (2007).

[31] I. Lindau and W. E. Spicer, Journal of Applied Physics **45**, 3720 (1974), https://doi.org/10.1063/1.1663849.

[32] J. M. Martinis, K. B. Cooper, R. McDermott, M. Steffen, M. Ansmann, K. D. Osborn, K. Cicak, S. Oh, D. P.

Pappas, R. W. Simmonds, and C. C. Yu, Phys. Rev. Lett. **95**, 210503 (2005).
[33] E. Sheridan, T. F. Harrelson, E. Sivonxay, K. A. Persson, M. V. P. Altoé, I. Siddiqi, D. F. Ogletree, D. I. Santiago, and S. M. Griffin, "Microscopic theory of magnetic disorder-induced decoherence in superconducting nb films," (2021), arXiv:2111.11684 [cond-mat.supr-con].
[34] A. Sundaresan, R. Bhargavi, N. Rangarajan, U. Siddesh, and C. N. R. Rao, Phys. Rev. B **74**, 161306 (2006).
[35] R. J. Cava, B. Batlogg, J. J. Krajewski, H. F. Poulsen, P. Gammel, W. F. Peck, and L. W. Rupp, Phys. Rev. B **44**, 6973 (1991).

APPENDIX

A. Orientation Map

Qualitative orientation maps were constructed using a custom algorithm, which employs a 1D annular virtual detector with a reciprocal length matching a known lattice reflection. Within the ring, the point of maximum intensity is collected, and its relative position, and thus angle, is used to show rotation between nearest pixels. To account for six-fold inherent symmetry associated with the {111} zone axis of niobium, angles are divided by 6. This method assumes relative out of plane alignment between grains and only within plane rotation.

B. Fluctuation Electron Microscopy

Analysis of scanning diffraction-based fluctuation electron microscopy measurements was performed using the MATLAB scripts provided by Kennedy *et al.* [27]. First, the background in the obtained diffraction patterns were removed by subtracting diffraction patterns taken from the vacuum region away from the sample. Upon obtaining these background subtracted diffraction patterns from the regions of interest, the resultant datasets were binned linearly to increase the signal-to-noise ratio. These binned scanning nanodiffraction image were fit radially using least squares fitting of the first diffraction ring. The radial intensity and normalized variance of the annular means were then calculated as a function of scattering angle. Due to minimal symmetry in the surface oxide, the inverse of the peaks in the normalized variance were used to estimate bond distances as a function of position.

I. SUPPLEMENTARY FIGURES

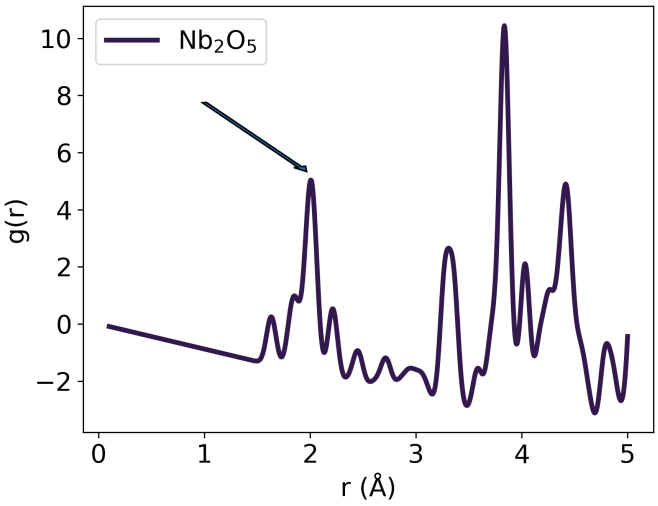

Figure S1. Radial distribution function of Nb_2O_5 calculated using PDFgui with feature at 2Å indicated [30].

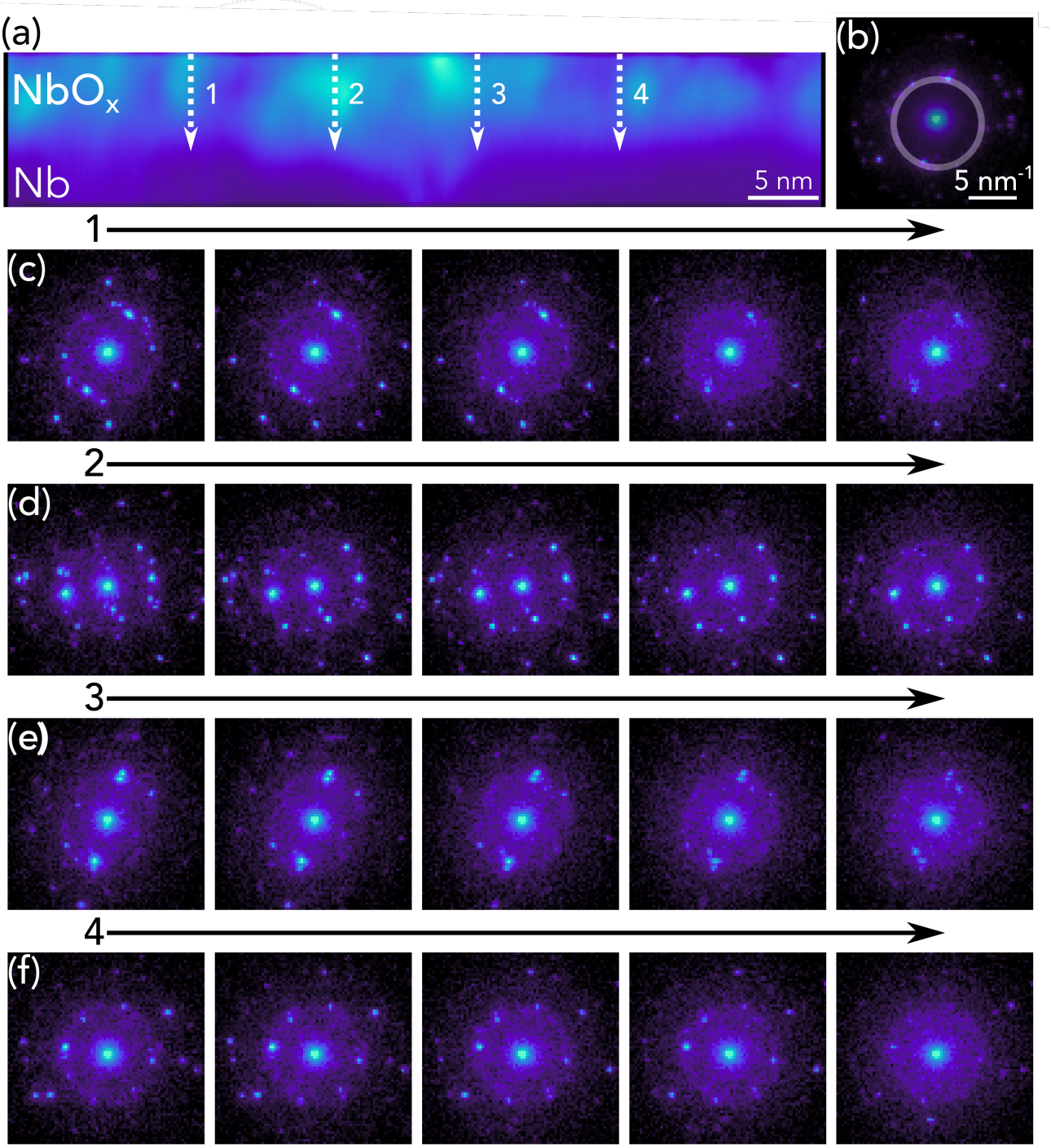

Figure S2. (a) DF image of Nb oxide/Nb constructed using a virtual detector that matched the diffraction ring of Nb oxide. The dotted arrows indicate regions over which changes in the diffraction pattern are provided in (c-f). (b) Diffraction pattern taken from NbO_x with a virtual annular detector with an inner collection angle of 10 mrad and an outer collection angle of 15 mrad to preferentially produce a NbO_x dark field image. (c-f) Evolution of the electron diffraction pattern in the direction of the arrows indicated in (a) for the labeled regions 1, 2, 3, 4, and 5, respectively. In all cases, prominent diffraction spots tend to decay in intensity when moving away from the surface.

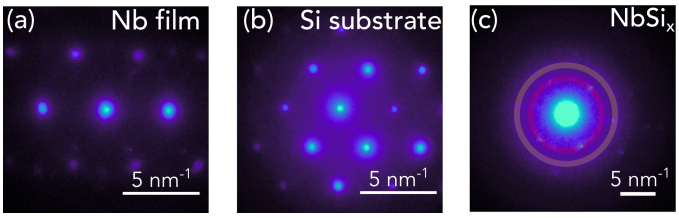

Figure S3. (a) Representative diffraction pattern taken from Nb thin film when oriented along the {111} zone axis and (b) representative diffraction pattern from the Si substrate oriented along the {111} zone axis. (c) Diffraction pattern taken from $NbSi_x$ with virtual annular detectors with collection angles of 20-25 mrad (red) and 40-45 mrad (orange). These detectors were used to produce the phase map in Figure 4a where the red detector was used to capture signal from Si and the orange detector was used to capture signal from Nb.